Surface Science 640 (2015) 50–58

Contents lists available at ScienceDirect

Surface Science

journal homepage: www.elsevier.com/locate/susc

Novel 2D RuPt core-edge nanocluster catalyst for CO electro-oxidation

Lars C. Grabow [a,*], Qiuyi Yuan [b], Hieu A. Doan [a], Stanko R. Brankovic [a,b,**]

[a] Department of Chemical and Biomolecular Engineering, University of Houston, Houston, TX 77204, USA
[b] Department of Electrical and Computer Engineering, University of Houston, Houston, TX 77204, USA

ARTICLE INFO

Available online 3 April 2015

Keywords:
CO oxidation
Core-edge nanocluster
Finite size effect
Galvanic displacement
Density functional theory
Electrocatalysis

ABSTRACT

A single layer, bi-metallic RuPt catalyst on Au(111) is synthesized using surface limited red-ox replacement of underpotentially deposited Cu and Pb monolayers though a two-step process. The resulting 2D RuPt monolayer nanoclusters have a unique core-edge structure with a Ru core and Pt at the edge along the perimeter. The activity of this catalyst is evaluated using CO monolayer oxidation as the probe reaction. Cyclic voltammetry demonstrates that the 2D RuPt core-edge catalyst morphology is significantly more active than either Pt or Ru monolayer catalysts. Density functional theory calculations in combination with infra-red spectroscopy data point towards oscillating variations (ripples) in the adsorption energy landscape along the radial direction of the Ru core as the origin of the observed behavior. Both, CO and OH experience a thermodynamic driving force for surface migration towards the Ru-Pt interface, where they adsorb most strongly and react rapidly. We propose that the complex interplay between epitaxial strain, ligand and finite size effects is responsible for the formation of the rippled RuPt monolayer cluster, which provides optimal conditions for a quasi-ideal bi-functional mechanism for CO oxidation, in which CO is adsorbed mainly on Pt, and Ru provides OH to the active Pt-Ru interface.

1. Introduction

Metal monolayers represent two-dimensional (2D) guest/host structures with fundamental and practical importance in the fields of electrocatalysis and fuel cells [1–10] as well as in gas-phase heterogeneous catalysis [11–16]. Their properties differ significantly from the corresponding bulk materials due to diverse structural and quantum effects [7,8,11,17–22]. In the monolayer (ML) configuration a guest metal forms nanoclusters of atomic height on the surface of a host metal up to the limit of a continuous overlayer. All guest atoms in the ML are exposed on the surface and experience the effect of the host substrate directly. The interaction between guest and host is manifested through structural contributions as epitaxial strain in the ML [2,19,20] and through a ligand effect, *i.e.* the d-electrons' orbital mixing between the guest ML and the host [4,10,11,18,20]. According to modern theoretical considerations the energy of the *d*-band center relative to the Fermi level is a suitable descriptor of the resulting catalytic behavior of the ML surface [22,23]. In the case of host substrates, which are weak ligands, the *d*-band center position is mainly affected by the level of coherent strain [19,23]. Positive (tensile) strain results in an upward shift of the *d*-band center position towards the Fermi level and increased reactivity of the ML [24,25]. If the strain is negative (compressive), the opposite effect transpires. For host substrates, which are strong ligands, the ligand and strain effects are coupled and the net shift in the *d*-band center energy is a convolution of both [11,20,22,23,26]. We have recently demonstrated that, for monolayer catalysts below the continuous coverage limit, the size of the 2D guest nanoclusters also plays an important role in their overall catalytic behavior (finite size effect) [27]. In such a ML catalyst morphology consisting of 2D nanoclusters with a certain size, the active (or residual) strain, ε, in a nanoclusters is a linear combination of the epitaxial strain, e, and the strain caused by the finite size effects [28–30]. Hence, the active strain in a 2D nanocluster has a radial dependence and is more compressive at the periphery than in the center of the cluster [27,30]. For very small clusters, the contribution of the size dependent compressive strain component is significant and the active strain in the nanocluster can differ considerably from the one set by the epitaxial relation between the guest ML and the host substrate [27]. This fundamental effect can be used as additional knob to fine tune ML catalysts' properties by control of their morphology [31–33].

The work presented here is the next step in our quest for a better and more sophisticated ML catalyst design. We synthesized a novel, bi-metallic RuPt ML catalyst on Au(111) having Ru-metal as a core and Pt-metal at the edge along the perimeter. We term this 2D ML nanocluster catalyst structure a "*core-edge*" configuration ($RuPt_{ML\text{-}CE}$/Au(111)). Cyclic voltammetry data for CO stripping (CO ML electro-oxidation) as a model reaction demonstrate that the bi-metallic $RuPt_{ML\text{-}CE}$/Au(111) catalyst is significantly more active than either

* Corresponding author.
** Correspondence to: S.R. Brankovic, Department of Chemical and Biomolecular Engineering, University of Houston, Houston TX, 77204.
E-mail addresses: grabow@uh.edu (L.C. Grabow), SRBrankovic@uh.edu (S.R. Brankovic).

http://dx.doi.org/10.1016/j.susc.2015.03.021
0039-6028/

Pt_{ML}/Au(111) or Ru_{ML}/Au(111) catalysts. Infra-Red Spectroscopy (IRS) and periodic Density Functional Theory (DFT) calculations point to a rich adsorption energy landscape of the $RuPt_{ML\text{-}CE}$ nanocluster as the origin of the exceptional activity. The unique interplay of a large epitaxial lattice constant mismatch, weak ligand effects, and strong finite size effects lead to a surface reconstruction characterized by ripples, which are comparable to those observed on fluid interfaces that are dominated by surface tension, *e.g.*, water/air [36]. We calculated that the resulting electronic structure variations along the radial direction of the Ru core provide a thermodynamic driving force for surface bound species to migrate to the catalytically active Ru-Pt interface. We propose that the combination of surface diffusion and interface kinetics leads to a quasi-ideal bi-functional mechanism for CO oxidation on $RuPt_{ML\text{-}CE}$/Au(111) with very high activity.

2. Experimental and computational methods

2.1. Catalyst synthesis

The Au(111) single crystal disk, 10 mm in diameter and 2 mm in thickness (Monocrystals Company), is prepared using several steps including mechanical polishing, electropolishing and hydrogen flame annealing [32]. Special attention is paid to avoid thermal reconstruction of Au(111) and consequent appearance of Au clusters on the surface upon immersion into the electrolyte. All solutions used in our experiments are made from ultra-high purity chemicals (99.999%, Alfa Aesar, Merck) and 18.2 MΩ ultrapure water (Millipore Direct Q-UV with Barnstead A1007 pre-distillation unit). All potentials related to the UPD experiments are referenced as the value of underpotential (ΔE). The potentials in IR experiments are quoted with respect to a saturated calomel electrode (SCE). The Pt_{ML}/Au(111) and Ru_{ML}/Au(111) catalysts are deposited via surface limited red-ox reduction (SLRR) of Cu_{UPD}/Au(111) [34,35]. To synthesize Cu_{UPD}/Au(111) a complete ML of Cu is deposited onto Au(111) at 30 mV underpotential from 10^{-3} M Cu^{2+} + 0.1 M $HClO_4$ solution. At these conditions, the Cu UPD ML forms a 2x2 structure on Au(111) with a coverage of 0.75 [37,38]. The SLRR solution for Pt or Ru ML deposition was 0.1 M $HClO_4$ with 10^{-3} M concentration of Pt(IV) or Ru(III) salts (K_2PtCl_6 or $RuCl_3$). Under these conditions, the lack of complexing ability of supporting electrolyte to Cu ions results in the situation where the main ligand of Cu ions is Cl^- liberated from the depositing Pt and Ru ions. Therefore, the proposed stoichiometry of SLRR reactions assumes Cu^+ as the stable and predominant oxidation state of Cu ion, and the expected Pt and Ru ML coverage of Au(111) is shown below [38]:

$$0.75Cu_{UPD}/Au(111) + 0.75\,\frac{1}{4}Pt^{4+} = 0.75Cu^{+} + 0.18Pt_{ML}/Au(111) \quad (1)$$

$$0.75Cu_{UPD}/Au(111) + 0.75\frac{1}{3}Ru^{3+} = 0.75Cu^{+} + 0.25Ru_{ML}/Au(111) \quad (2)$$

The $RuPt_{ML\text{-}CE}$/Au(111) catalyst is deposited using a slightly more complex procedure. First, the Ru_{ML}/Au(111) is deposited as described above. In the second step, a small amount of Pb is deposited via UPD on Ru_{ML}/Au(111) at 275 mV underpotential. The Pb atoms are then replaced by Pt using either 10^{-3} M K_2PtCl_6 + 0.1 M $HClO_4$ or 10^{-3} M K_2PtCl_4 + 0.1 M $HClO_4$ solutions. All UPD and SLRR solutions were de-aerated with ultra-pure argon for 2 hours before the experiments.

2.2. Surface characterization and activity testing

All electrochemical experiments, including the *ex-situ* and *in-situ* scanning tunneling microscopy (STM) studies, are performed in a nitrogen-purged glove box. For the CV measurements for CO ML electro-oxidation (for brevity we simply use the term "CO oxidation" in the text), the catalyst surface is initially saturated with CO at −100 mV vs. SCE from a CO-saturated 0.1 M $HClO_4$ solution at room temperature and ambient pressure. The solution is then purged for 2 hours with N_2 to remove any excess CO from the bulk solution before the start of each CV or IR measurement. The sweep rate was 50 mVs^{-1}. After each deposition experiment, a number of STM images are recorded. The STM images are recorded using Nanoscope V controller with multimode scanner unit (Veeco Instruments) and analyzed using our custom made digital image processing algorithm [39,40]. In the case of Pb UPD on Ru_{ML}/Au(111), *in-situ* STM measurements were obtained to elucidate the mechanistic details and morphology change during the initial stage of Pb UPD. The STM image analysis provided information about 2D nanocluster nucleation density, average size, coverage, and the nanoclusters height. Image segmentation is used for differentiation and identification of each nanocluster on the image/surface. For this purpose, a threshold value has been determined to segment each image into a binary image using an autonomous global thresholding method [41]. The error bar for image analysis results represents the standard deviation of the data obtained from analysis of all images used for a particular experiment.

The cell for *in-situ* IR spectro-electrochemical measurements, described previously [42], consisted of a ZnSe hemisphere serving as the attenuated total reflection (ATR) window and cell bottom, and a Teflon body. A Nicolet 6700 spectrometer and a BAS CV27 potentiostat are used to conduct our experiments. The collection of the spectra is computer controlled at a given potential of the working electrode set prior to data acquisition. The 128 scans with 4 cm^{-1} resolution are co-added in a single step. Spectra are given as -ΔR/R using the spectrum at the highest potential as the reference one where no CO adsorption occurs. The positive-going bands therefore represent a gain of a particular species at the sample potential relative to that at the reference potential.

2.3. Computational methods

Periodic density functional theory (DFT) calculations were performed using the Vienna ab-initio simulation package (VASP) [43,44] in the projector augmented wave (PAW) [45,46] formulation and a kinetic energy cutoff of 400 eV. The revised Perdew-Burke-Ernzerhof (GGA-RPBE) functional [47] was used to describe exchange and correlation. A Gaussian smearing with a Fermi temperature of $k_bT = 0.1$ eV was employed and the total energy was subsequently extrapolated to $k_bT = 0.0$ eV [48]. For geometry optimizations, forces were converged below 0.05 eV/Å. All surface models were built within the Atomic Simulation Environment (ASE) [49]. Surfaces of Pt(111) and Ru(111) were modeled as five-layer fcc(111) slabs, where the top three layers were relaxed and the bottom two layers were fixed in their bulk positions. We used Ru(fcc) instead of Ru(hcp) as reference material to eliminate any effects caused by crystal structure changes when Ru is forced into the fcc symmetry when present as ML on the Au fcc host. The theoretically obtained lattice constants of 3.998 Å, 3.836 Å, and 4.215 Å were found for Pt, Ru(fcc), and Au, respectively. These lattice constants correspond to atom-atom distances in the closed packed (111) plane of 2.83 Å, 2.69 Å, 2.98 Å and are in reasonable agreement with the experimental values of 2.78 Å, 2.65 Å (hcp), and 2.88 Å for Pt(111), Ru(0001), and Au(111) [50]. Calculations for Pt(111) and Ru(111) were performed in a (3x3) unit cell with a (4×4×1) Monkhorst-Pack k-point [51] mesh. Slabs were separated with a vacuum spacing of 14 Å along the normal (z) direction of the surface. The monolayer core-edge system $RuPt_{ML\text{-}CE}$/Au(111) was modeled as 37 atom cluster consisting of a Ru island surrounded by Pt atoms at the perimeter, supported on a (10×10) unit cell of Au(111) with four atomic layers. A VASP POSCAR file ("RuPt_Au111_POSCAR") of the relaxed $RuPt_{ML\text{-}CE}$/Au(111) structure is provided in the Supplementary material. The size of the RuPt core-edge cluster is approximately 1.5 nm in diameter. Gamma-point only calculations of $RuPt_{ML\text{-}CE}$/Au(111) were performed with the same constraints and vacuum separation as in the (3×3)

unit cells. A dipole correction [52] to the electrostatic potential was included to separate adjacent unit cell images. Binding energies for CO and OH are provided with reference to the relaxed surface and the gas-phase species CO, H_2O and H_2.

3. Results

3.1. Pb UPD on Ru_{ML}/Au(111) and $RuPt_{ML\text{-}CE}$/Au(111) synthesis

The prelude for $RuPt_{ML\text{-}CE}$/Au(111) catalyst synthesis is Pb UPD on Ru_{ML}/Au(111). This process is examined in more detail by CV and STM in order to provide sufficient evidence for the formation of a core-edge structure of $RuPt_{ML\text{-}CE}$/Au(111). The CV data for Pb UPD on Ru_{ML}/Au(111) are shown in Fig. 1A. The overall features of the voltammogram are very similar to the standard Pb UPD on Au(111). However the larger cathodic current and sub peak are observed at higher underpotentials ($\Delta E > 250$ mV) due to a larger population of defects such as Ru nanocluster edges where the initial UPD process starts. The onset of the UPD process starts with a broad cathodic peak shoulder evident at $\approx$ 510 mV ΔE. The main UPD features are associated with the sub peak centered at $\approx$ 250 mV and the main deposition peak at $\approx$ 190 mV ΔE. The *in-situ* STM images recorded during Pb UPD on Ru_{ML}/Au(111) are shown in Fig. 1B with the corresponding underpotentials annotated in the upper right corners. The quantitative analysis of these images is presented in Fig. 2A-C. The initial Ru_{ML}/Au(111) surface at 600 mV ΔE has a Ru nanocluster population on Au(111) with 23 % coverage and an average size of 12 $\pm$ 3.0 nm^2. The Ru ML coverage observed by STM is in good agreement with the coverage expected from the SLRR reaction stoichiometry, Eq. (2). The cathodic sweep towards 400 mV ΔE does not produce any appreciable change on Ru_{ML}/Au(111). Analog to the Pb UPD on Au(111), the cathodic current in the range 400 mV < ΔE < 500 mV is most likely associated with Pb UPD on defects sites of the Au(111) surface [40].

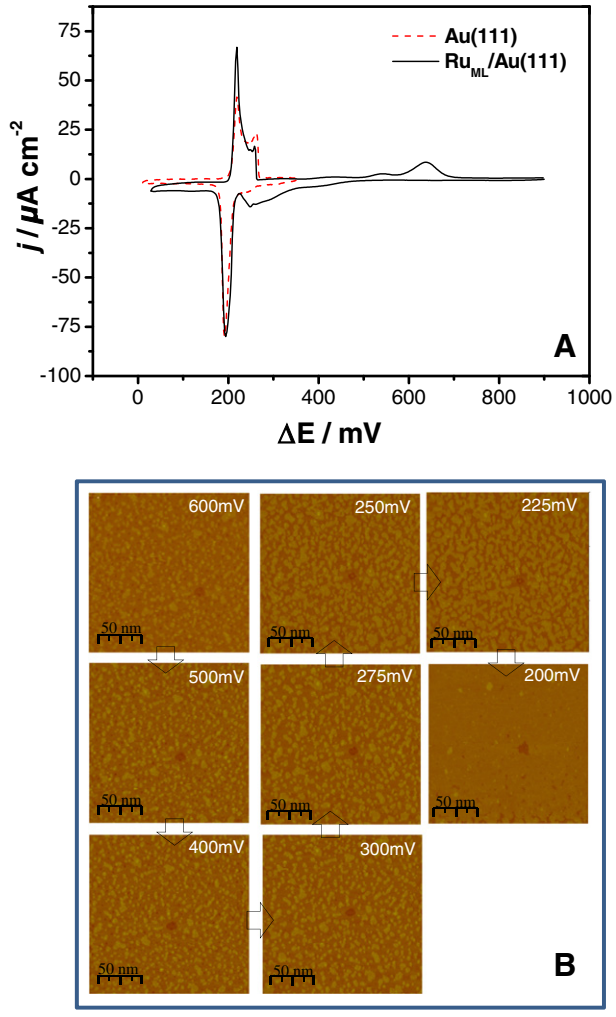

Fig. 1. (A) Cyclic voltammogram of Pb UPD on Au(111) (dotted red) and on Ru_{ML}/Au(111) (solid black). Sweep rate 10 mVs^{-1}, solution: 10^{-3} M Pb^{2+} + $HClO_4$. (B) The STM image sequence recorded *in-situ* during Pb UPD on Ru_{ML}/Au(111). The arrows in (B) indicate potential and temporal sequence of recorded STM images.

Further sweep of the potential in cathodic direction produces a noticeable change in the Ru_{ML}/Au(111) surface morphology. Below 300 mV ΔE, the 2D Ru nanoclusters start to show lateral growth quantified by an increase in their average size, Figs. 1B and 2C. Concurrently, the surface coverage of the 1st layer starts to increase and the cluster density starts to decrease, Fig. 2A and C. These data suggest that Pb UPD on Ru_{ML}/Au(111) proceeds by edge decoration of Ru nanoclusters with Pb adatoms, which appears as their lateral growth, *i.e.* the growth of PbRu nanoclusters. The process is schematically depicted in Fig. 2D. At 250 mV ΔE we observe the onset of nucleation of a 2nd Pb UPD layer on top of Ru nanoclusters (Figs. 1B and 2A-C).

A further decrease of the underpotential and entering the main UPD peak at ΔE = 200 mV results in formation of a continuous Pb UPD layer on Au(111). This is evident by coalescence of growing PbRu nanoclusters into a complete 1st layer while the properties of the 2nd layer (on top of Ru) remain more or less constant, Fig. 2A-C. Clearly, the interesting underpotential region for the preparation of core-edge nanoclusters is the range between 300 mV and 250 mV ΔE (shaded regions, Fig. 2). The Pb decorated Ru nanoclusters formed in this region provide a unique starting configuration that can be used for design and synthesis of bi-metallic PtRu nanoclusters with the desired core-edge structure. Indeed, this can be achieved by performing a second SLRR reaction between the Pb ad-atoms within the PbRu nanocluster and Pt ions. The general idea is outlined as cartoon in Fig. 3. We note that the amount of deposited Pt at the perimeter of Ru nanoclusters is dependent on the SLRR reaction stoichiometry, *i.e.* the oxidation state of Pt ions (Pt^{n+}), and the amount of Pb decorating the perimeter of Ru nanoclusters. The latter one depends on the ΔE chosen for Pb UPD, which we fixed at ΔE = 275 mV for the following reasons. First, this potential is the lowest underpotential at which the growth of a 2nd Pb layer on top of the Ru nanoclusters is not observed. This implies that the PbRu nanoclusters maintain their 2D configuration, Figs. 1B and 2A-C. Second, at this underpotential, the amount of Pb contained in the PbRu nanoclusters is truly limited to a decoration of the Ru nanoclusters' perimeter. Therefore, the same is expected for Pt deposited via the SLRR reaction. Further support for this interpretation is provided by our STM image analysis in Fig. 2C, which indicates that at ΔE = 275 mV the Ru nanoclusters' average size increases from initially 12 $\pm$ 3 nm^2 (Ru_{ML}/Au(111)) to 21 $\pm$ 1 nm^2 (Pb_{UPD}/Ru_{ML}/Au(111)@ ΔE = 275 mV). Assuming a compact nanocluster shape this corresponds to an increase of the nanoclusters' radius from $R_{Ru} \approx 2$ nm to $R_{PbRu} \approx 2.6$ nm. The diameter of a Pb atom is $\approx$ 0.35 nm [50] and the difference between R_{Ru} and R_{PbRu} of $\approx$ 0.6 nm suggests that, on average, each Ru nanocluster has a continuous belt of Pb atoms at its perimeter, which is between one and two Pb atoms wide, Fig. 3-schematics.

Based on these considerations, we can expect that Pt will deposit also as continuous belt around the perimeter of a Ru nanocluster (SLRR solution with Pt^{2+}), or as an incomplete fractional decoration of the Ru nanoclusters' edge (SLRR solution with Pt^{4+}), Fig. 3-schematics. To provide further support for the formation of core-edge structures we include a representative STM image of $RuPt_{ML\text{-}CE}$/Au(111) in Fig. 3, which is obtained by SLRR of Pb_{UPD}/Ru_{ML}/Au(111)@275 mV ΔE. The SLRR solution contained Pt^{2+}. The presence of a 2nd layer on some nanoclusters is evident and additional population of smaller nanoclusters in the 1st layer, suggesting that besides a direct Pb-Pt redox replacement, a local galvanic-cell mechanism for Pt deposition operates but to rather minor extent [34]. The STM characterization of

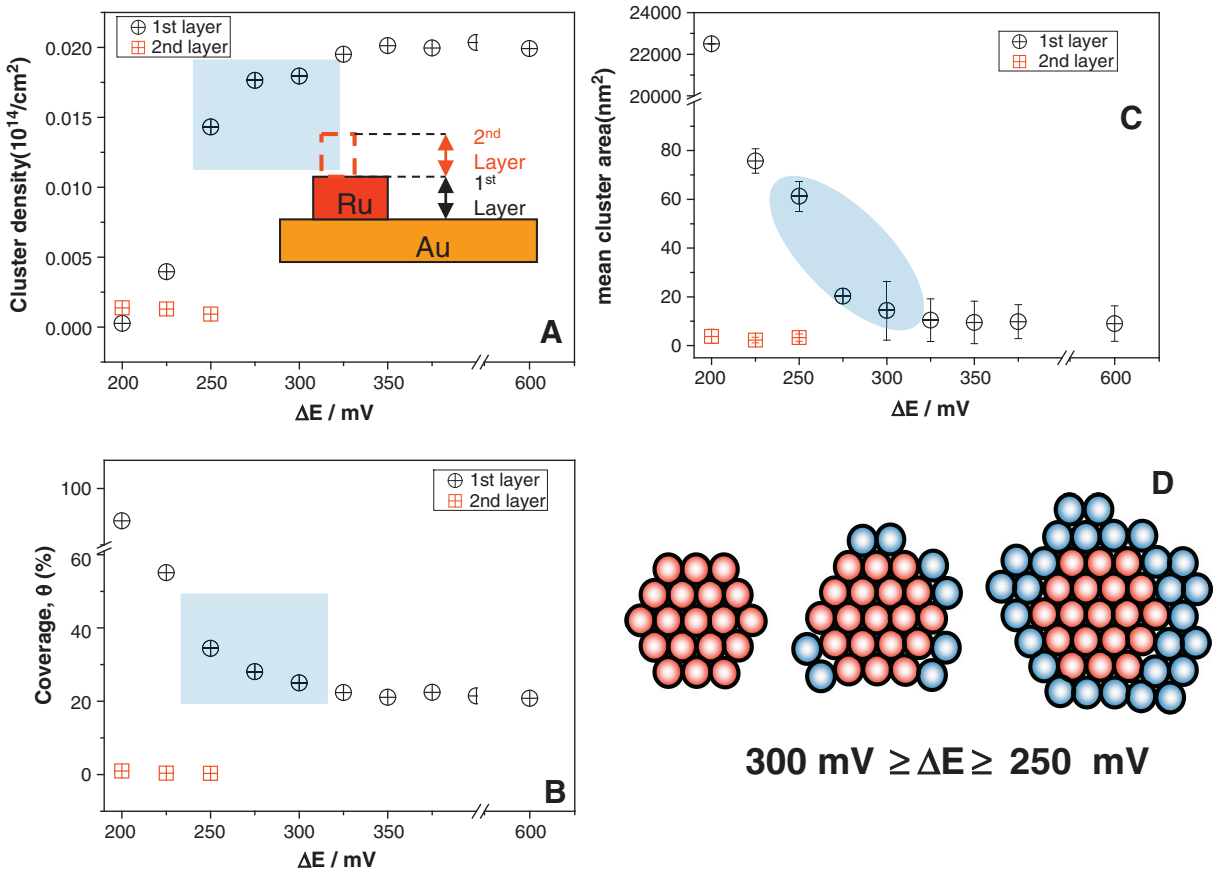

Fig. 2. Results from STM image analysis: (A) nanocluster density vs. ΔE, inset shows the model with notation for the layers, (B) nanocluster coverage vs. ΔE, (C) mean nanocluster size vs. ΔE. (D) Schematic representation of the PbRu nanclusters (Ru – red, Pb – blue) corresponding to the shaded area in graphs (A–C).

$RuPt_{ML\text{-}CE}/Au(111)$ shows that the average size of a PtRu nanocluster is $\approx 19 \pm 0.6$ nm^2. This corresponds to a radius of $R_{PtRu} \approx 2.45$ nm. The size reduction of PtRu nanoclusters compared to the initial PbRu morphology ($R_{PtRu} \approx 2.45$ nm vs. $R_{PbRu} \approx 2.6$ nm.) is expected. Some loss of Pb on the surface during SLRR is possible due to the presence of residual O_2 in solution ($<10^{-6}$ M) and thus, less Pt is deposited than expected from the SLRR reaction stoichiometry. In an ideal one-to-one exchange between Pb and Pt during the SLRR reaction, the smaller radius of PtRu nanoclusters is expected also as a result of smaller Pt atoms replacing larger Pb atoms at the nanocluster perimeter. Indeed, the observed difference between R_{PtRu} and R_{PbRu} of 0.15 nm is very close to the calculated difference in dimensions between Pt and Pb two-atom wide perimeters decorating Ru nanoclusters ($2(d_{Pb}\text{-}d_{Pt}) = 0.158$ nm).

3.2. CO monolayer (ML) oxidation

The CVs for CO ML electro-oxidation on different Ru and Pt morphologies on Au(111) are shown in Fig. 4. In Fig. 4A, we compare two different $RuPt_{ML\text{-}CE}/Au(111)$ catalyst morphologies, in which the blue (black) line indicate data for the $RuPt_{ML\text{-}CE}/Au(111)$ catalyst obtained from

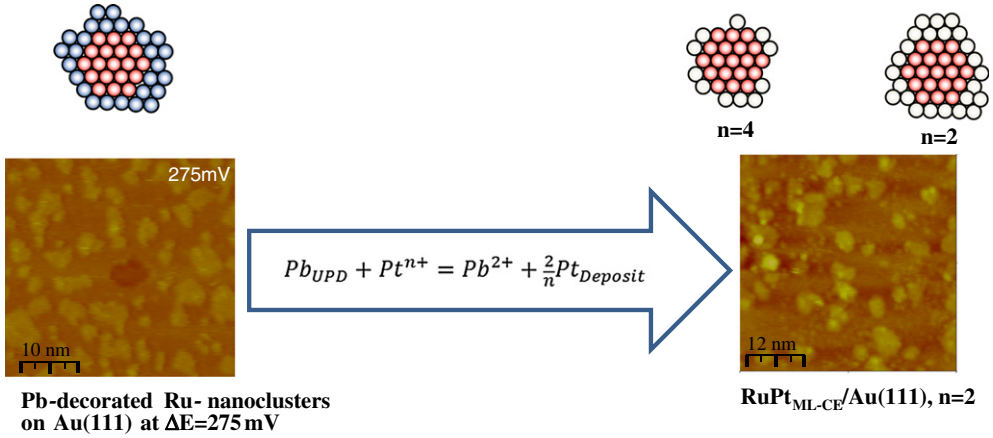

Fig. 3. Representative STM image of the surface morphology for (left) $Pb_{UPD}/Ru_{ML}/Au(111)$@ΔE = 275 mV, and (right) $RuPt_{ML\text{-}CE}/Au(111)$ obtained from SLRR solution containing Pt^{2+}. The cartoons above the STM images illustrate the proposed nanocluster structures (Ru – red, Pb – blue, Pt – light gray, *n* – oxidation state of Pt^{n+} ion). The SLRR reaction stoichiometry within the arrow indicates the process causing the morphology change from left to right.

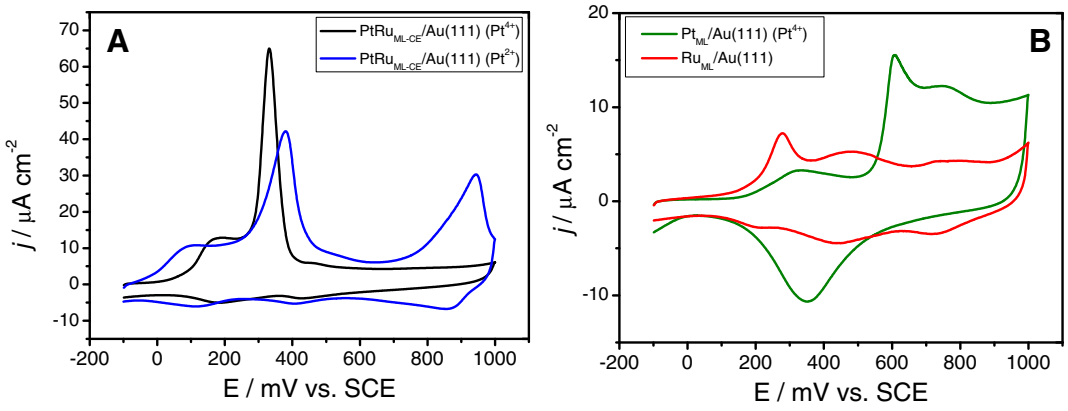

Fig. 4. Cyclic voltammogram (CV) for CO oxidation on (A) $RuPt_{ML\text{-}CE}/Au(111)$ and (B) $Pt_{ML}/Au(111)$ and $Ru_{ML}/Au(111)$. Solution: 0.1 M $HClO_4$, sweep rate 50 mVs^{-1}, CO ML adsorbed at −100 mV, upon which the solution is purged for 2 hours with N_2.

SLRR solution containing Pt^{2+} (Pt^{4+}) ions. In Fig. 4B the CVs for CO oxidation on $Pt_{ML}/Au(111)$ (green), and $Ru_{ML}/Au(111)$ (red) catalysts are shown as reference. The very early onset of CO oxidation (E < 100 mV) on both $RuPt_{ML\text{-}CE}/Au(111)$ catalysts is quite remarkable and significantly lower than either $Pt_{ML}/Au(111)$ or $Ru_{ML}/Au(111)$. The positive charge under the main anodic peaks, which correspond to CO oxidation (300 mV < E < 350 mV), is comparable for these two configurations (110 μC·cm^{-2} for black and 130 μC·cm^{-2} for blue curve). As expected, the configuration with more Pt also has a larger anodic charge related to CO stripping. For both Ru-$Pt_{ML\text{-}CE}/Au(111)$ configurations the CO stripping charge is slightly larger than one would expect based on the geometrical coverage of the Au surface by Pt-Ru clusters (≈30 %) [53,54], which suggests that the Pt perimeter of the $RuPt_{ML\text{-}CE}$ clusters, i.e. Pt steps on Au(111), may serve as additional adsorption sites for CO. The potential of the main CO oxidation peak for both $RuPt_{ML\text{-}CE}/Au(111)$ catalysts (340 mV black and 380 mV blue line) is shifted to slightly more positive potentials than on $Ru_{ML}/Au(111)$ (290 mV red line, Fig. 4B) or on a polycrystalline PtRu alloy with 1:1 atomic ratio [55]. The CO oxidation peaks for both $RuPt_{ML\text{-}CE}/Au(111)$ catalysts share a common characteristic current plateau feature appearing before the main CO oxidation peak. The magnitude of the current in the plateau region is approximately equal ($j \approx 10$ μAcm^{-2}) for both configurations. This is an interesting result which indicates that, in the initial stage of CO oxidation on $RuPt_{ML\text{-}CE}/Au(111)$ surfaces, the reaction is not kinetically limited but rather transport controlled. Transport limitations for CO adsorption from solution can be excluded, because the CO ML is already pre-adsorbed on the catalyst surface and it is the only CO present [55]. Hence, the transport limitations must originate from surface diffusion of one or more reacting species to a catalytically active site.

Further investigation of the data in Fig. 4A indicates that $RuPt_{ML\text{-}CE}/Au(111)$ (Pt^{2+}) with more Pt at the perimeter appears to be more active, *i.e.*, the onset of CO oxidation is observed at 100 mV more negative potential (E ≈ 0 mV) than for $RuPt_{ML\text{-}CE}/Au(111)$ (Pt^{4+}) with less Pt (E ≈ 100 mV). Approaching the anodic sweep limit, the same $RuPt_{ML\text{-}CE}/Au(111)$ (Pt^{2+}) catalyst also shows a reversible anodic/cathodic peak centered at E ≈ 900 mV, which is absent on the CV for $RuPt_{ML\text{-}CE}/Au(111)$ (Pt^{4+}) with less Pt at the perimeter. We associate this feature with the oxidation/reduction cycle of Pt, which is part of the $RuPt_{ML\text{-}CE}/Au(111)$ (Pt^{2+}) catalyst. This difference might indicate that Pt-like behavior tends to be preserved in $RuPt_{ML\text{-}CE}/Au(111)$ (Pt^{2+}) where Pt has a larger presence at the perimeter of the PtRu nanocluster. The earlier onset of CO oxidation could be also related to this structural difference.

In contrast, the CO stripping data in Fig. 4B for $Pt_{ML}/Au(111)$ and $Ru_{ML}/Au(111)$ show much lower activity. The magnitude of anodic currents related to CO oxidation are almost an order of magnitude lower as compared to $RuPt_{ML\text{-}CE}/Au(111)$. One possible reason for this difference could be the lower coverage of Ru (≈23%) and Pt (≈15%) of the Au(111) surface and therefore, a smaller total amount of adsorbed CO as compared to $RuPt_{ML\text{-}CE}/Au(111)$ (≈30%). However, the difference of peak currents between $Pt_{ML}/Au(111)$, $Ru_{ML}/Au(111)$ and $RuPt_{ML\text{-}CE}/Au(111)$ is significantly larger than the respective coverage difference, which suggests that other effects play a role. The $Pt_{ML}/Au(111)$ surface appears to have faster CO oxidation kinetics (higher current density *j*) than $Ru_{ML}/Au(111)$, although the main peak for CO oxidation occurs at much more positive potential (E = 650 mV for $Pt_{ML}/Au(111)$ vs. E = 290 mV for $Ru_{ML}/Au(111)$). The main peak position for $Ru_{ML}/Au(111)$, however, coincides roughly with the onset of the main peak for $RuPt_{ML\text{-}CE}/Au(111)$, indicating that the reacting species on $Ru_{ML}/Au(111)$ and $RuPt_{ML\text{-}CE}/Au(111)$ are thermodynamically equivalent. The drastic increase in CO oxidation kinetics on $RuPt_{ML\text{-}CE}/Au(111)$ can only be attributed to reaction sites at the Pt-Ru interface, which are absent for $Pt_{ML}/Au(111)$ or $Ru_{ML}/Au(111)$.

3.3. Subtractively normalized Fourier transform infra-red spectroscopy (SNFTIRS) results

An adsorbed CO molecule forms σ and π bonds with a transition metal surface (Pt and Ru). The π bond represents sizable contribution to the adsorption energy [23,56], and is formed by back donation of metal *d*-electrons into the π*−antibonding molecular orbital of CO. Changes in the *d*-band center energy of a specific surface metal atoms (M) due to strain, ligand or 2D finite size effects influence the strength of M-CO and C = O bonds simultaneously [21]. A shift in *d*-band center energy of surface metal atoms can be assessed indirectly by observing changes in the C = O bond stretching frequency of an adsorbed CO molecule. More δ−π* back donation results in a stronger metal M-CO bond, but, at the same time, a weaker C = O bond, which lowers its stretch frequency. Hence, a shift of the C = O stretching band towards lower wave numbers can be qualitatively interpreted as an increase in M-CO bond strength as long as CO binds to the same type of metal [56]. A direct comparison of C = O stretch frequencies and binding strength between different metals, e.g. Pt and Ru, is unfortunately not feasible, because of other energetic contributions to the M-CO bond that are not captured by the δ−π* back donation model [23].

In Fig. 5, Subtractively Normalized Fourier Transform Infra−Red Spectroscopy (SNFTIRS) data are shown for CO adsorbed at 0.1 V vs. SCE on several different ML catalyst surfaces and Pt(111) as reference. The focus of our discussion is on the position of the stretching band of linearly bonded CO, ν_{CO}, which contains qualitative information pertaining to the binding preference and strength of CO on the $RuPt_{ML\text{-}CE}/Au(111)$ surface. In the case of $Ru_{ML}/Au(111)$, the main peak is asymmetric and observed at 2065 cm^{-1}. In close proximity to the main peak towards lower wave numbers a more complex peak

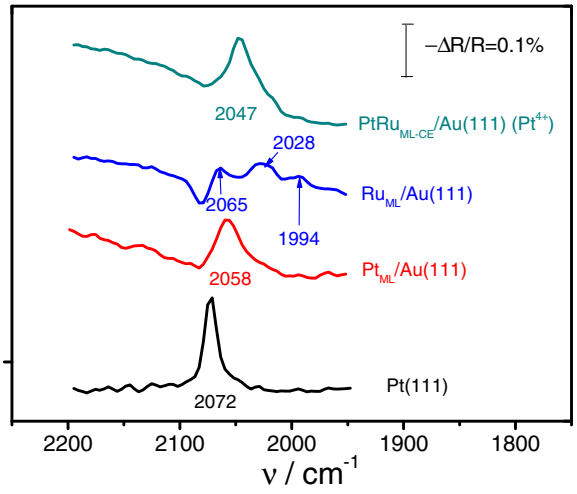

Fig. 5. SNFTIR spectra for CO adsorption on different ML catalysts and Pt(111). Spectra recorded at 100 mV in 0.1 M $HClO_4$ solution; reference spectra taken at 900 mV. Spectra are offset for clarity.

structure develops. We can discern two additional peaks at 2028 and 1994 cm^{-1}. The latter one is very weak and almost comparable to the noise level. A comparison to Ru(0001), $\nu_{CO} = 2011$ cm^{-1} [54], indicates that the two peaks above 2011 cm^{-1}, including the main peak, correspond to CO on Ru_{ML}/Au(111) that is more weakly bound than on Ru(0001). The small peak at 1994 cm^{-1} is consistent with a minority fraction of CO that is more strongly adsorbed than on Ru(0001). If we assume an epitaxial Ru ML on Au(111), the average strain in Ru nanoclusters is positive and a strain-only based argument predicts only stronger CO binding, the opposite of what our experiment shows. The non-intuitive observations of weaker binding and multiple SNFTIR peaks will be explained in the computational section and are caused by a reconstruction of the Ru cluster to form concentric ripples. The ν_{CO} for $RuPt_{ML-CE}$/Au(111) has a lower wave number (2047 cm^{-1}) than either Pt(111) (2072 cm^{-1}), Pt_{ML}/Au(111) (2058 cm^{-1}) or Ru_{ML}/Au(111) (2065 cm^{-1}), which is consistent with CO binding most strongly to $RuPt_{ML-CE}$/Au(111). We also observe a similar peak shape for $RuPt_{ML-CE}$/Au(111) and Pt_{ML}/Au(111).

3.4. Density functional theory (DFT) simulations

3.4.1. $RuPt_{ML-CE}$/Au(111) surface model

The idealized model of the $RuPt_{ML-CE}$/Au(111) surface used in our DFT analysis is shown in Fig. 6A,B after geometry relaxation. The Ru and Pt atoms in the initial configuration were placed in a planar geometry on top of the Au(111) surface and their lateral distance was determined by the Au lattice constant, *i.e.*, Ru and Pt experienced significant positive (expansive) lateral strain as determined by the lattice constant mismatch. On the basis of the calculated metal-metal atom distance, d_M, in the fcc(111) plane the expansive strain $e = \frac{d_{Au} - d_M}{d_M}$ was 9.9 % for M = Ru and 5.4 % for M = Pt. Using experimentally obtained values and the hcp(0001) plane for Ru as reference, the strain is less severe and reduces to 6.7 % for Ru and 3.9% for Pt [50]. The anticipated outcome with this initial configuration was a stretched out $RuPt_{ML-CE}$ nanocluster, which mostly assumes the Au lattice constant and exhibits reduced strain at the cluster perimeter due to compensation by finite size effects [28–30]. Upon optimization, however, the compressive finite size effects outweighed the expansive epitaxial strain and in combination with the weak ligand effect between Au and Ru or Pt, the initially stretched $RuPt_{ML-CE}$ nanocluster contracted to a final geometry with negative (compressive) strain. To quantify the compressive strain, we averaged the bond distances within each concentric ring of the model system, Fig. 6A, and related the change to the equilibrium lattice

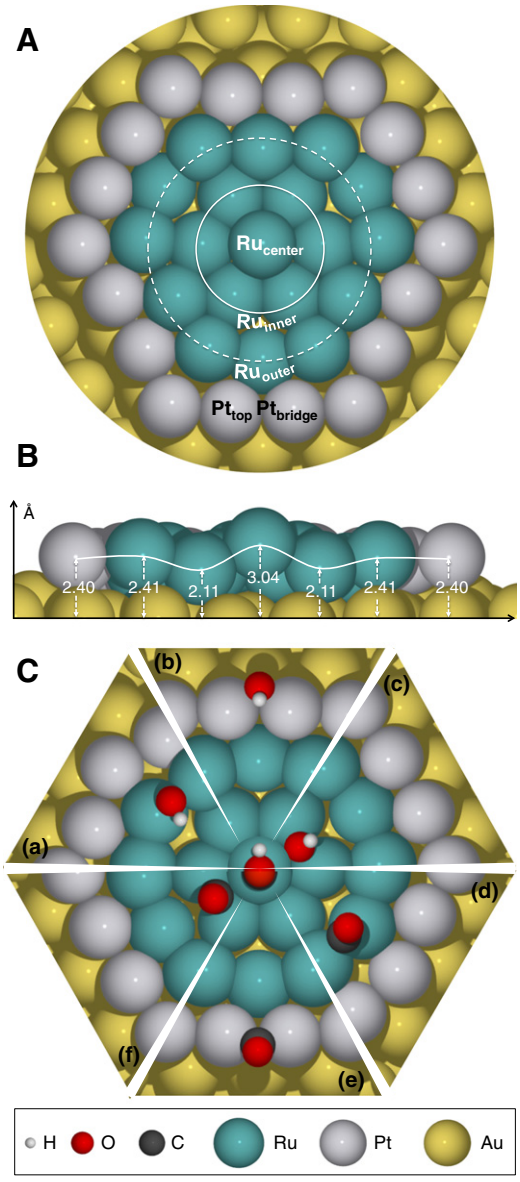

Fig. 6. DFT calculated equilibrium structures. (A) Top view and (B) cut through the center of a ca. 1.5 nm $RuPt_{ML-CE}$ cluster on Au(111). The average height of each concentric ring of Ru or Pt above the Au(111) surface is indicated in (B). (C) Position of the most stable calculated adsorption sites for OH (a-c) and CO (d-f) on the different concentric rings: a – OH on Ru_{outer}; b – OH on Pt; c – OH on Ru_{inner}; d – CO on Ru_{outer}; e – CO on Pt; f – CO on Ru_{inner}. Adsorption of OH/CO on the central Ru atom ($Ru_{central}$) is also depicted.

constant for the bulk fcc system. For the single Ru atom at the center, we considered its bond lengths to the surrounding six Ru atoms. From this analysis we obtain $\varepsilon = -0.4$ % for $Ru_{central}$, $\varepsilon = -6.7$ % for Ru_{inner}, $\varepsilon = -6.1$ % for Ru_{outer}, and $\varepsilon = -6.8$ % for Pt. Given that the model cluster radius of ca. 0.75 nm is smaller than the experimentally synthesized clusters ($R_{PtRu} \approx 2.45$ nm), the cluster contraction caused by finite size effects is likely overestimated in our simulations. Yet, during the optimization of a continuous Ru ML on Au(111) in a (3×3) unit cell, we also observed the contraction of the Ru layer and the formation of a patchy surface. Since the continuous overlayer is representative of a very large Ru particle, we can conclude from these results that the lattice constant mismatch between Ru and Au is too large and the ligand effect between Ru and Au too weak to maintain an epitaxial relationship at any cluster size. Hence, finite size effects can be expected to dominate in this system. This surprising result could not have been anticipated, but is important to understand the unique CO ML electro-oxidation behavior of this catalyst.

Associated with the strong $RuPt_{ML\text{-}CE}$ nanocluster compression we observe vertical rippling of the 2D cluster, Fig. 6B. In the final structure, the Ru core consists of alternating high and low concentric atomic rings, where the height variation is more pronounced towards the cluster center. The position of the $Ru_{central}$ atom is 0.93 Å higher above the Au(111) surface than the Ru_{inner} ring. By moving upwards the $Ru_{central}$ atom can escape the strong compression and reduce its local strain to −0.4 %. Ru atoms in the Ru_{outer} ring are only ca. 0.4 Å higher than Ru atoms in the Ru_{inner} ring and at approximately the same height as the surrounding Pt atoms. We find that the interplay between epitaxy, finite size and ligand effects in this system lead to a complex nanocluster structure with spatial variations in its geometry, and consequently, its catalytic behavior.

3.4.2. OH adsorption on $RuPt_{ML\text{-}CE}$/Au(111)

The reconstruction of the $RuPt_{ML\text{-}CE}$/Au(111) surface leads to a rich adsorption energy landscape for OH and CO as summarized in Table 1. The geometries of preferred binding configurations on each concentric ring of the $RuPt_{ML\text{-}CE}$/Au(111) surface are given in Fig. 6C. We find that OH binds very strongly to the elevated $Ru_{central}$ site and bridge sites on the raised Ru_{outer} ring. The most stable position for OH is on a bridging Ru_{outer} site located directly at the Ru-Pt interface of the core-edge structure, where it binds ca. 0.7 eV more strongly than on the Ru(111) surface. In contrast, the OH binding energy on bridge sites of the lower laying Ru_{inner} ring is 0.16 eV weaker than on Ru(111). Simple strain arguments would have suggested that the compressed Ru surface binds generally weaker than the equilibrated Ru(111) surface, but our DFT results indicate the presence of strong binding sites on the elevated and more exposed Ru atoms. This demonstrates that epitaxial strain arguments only apply to scenarios with no or moderate surface relaxation. OH binding to Pt is as unfavorable on the $RuPt_{ML\text{-}CE}$/Au(111) surface as it is on Pt(111) and no significant OH coverage on Pt sites can be expected. If one extrapolates these results to a larger, yet contracted, Ru_{ML}/Au(111) cluster, we expect that every other (elevated) row binds OH strongly, whereas the lower laying rows in between bind OH weaker than the Ru(111) surface. Thus, diffusion of adsorbed OH in the outward radial direction towards the strongly binding Ru-Pt interface is hindered by the rippled surface morphology. If we simply take the binding energy difference between OH adsorption on $Ru_{central}$ and Ru_{inner} as an estimate of the minimum required diffusion barrier, we obtain ca. 0.6 eV. With the addition of even just a small kinetic barrier this implies that OH is trapped at a certain distance from the nanocluster center and cannot easily diffuse along the radial direction or reach the Ru-Pt interface unless a sufficient potential is applied.

3.4.3. CO adsorption on $RuPt_{ML\text{-}CE}$/Au(111)

The reconstructed $RuPt_{ML\text{-}CE}$/Au(111) surface offers a variety of binding sites for CO as given in Table 1 and shown in Fig. 6C(d-f). CO adsorption on a top site of the Pt ring ($E_{CO} = -2.02$ eV) is stronger than on a top site of Pt(111) ($E_{CO} = -1.73$ eV). If CO adsorbs on a Pt_{bridge} site of $RuPt_{ML\text{-}CE}$/Au(111), Fig. 6C(e), its binding strength increases to $E_{CO} = -2.12$ eV. The bridge site is also the preferred site for CO adsorption on the outer and inner Ru ring. Before we continue the presentation of the CO adsorption results, we need to address the well-documented problem of standard GGA-DFT methods to predict correct adsorption site preferences and its implication for the present study [57,58]. The SNFTIRS data in Fig. 5 provide experimental evidence for on-top adsorption of CO on $RuPt_{ML\text{-}CE}$/Au(111) and show the ν_{CO} signal associated with on-top adsorbed CO. The maximum difference between on-top and bridge adsorption in Table 1 is 0.18 eV for Ru_{inner} and less than 0.1 eV for all other locations. The narrow preference between these high symmetry sites is consistent with a previous DFT study [59]. As it turns out, it does not matter if we base our radial adsorption analysis given below on the most stable CO adsorption site according to DFT, *e.g.* bridge, or by restricting CO adsorption to the experimentally observed on-top positions only. For complete transparency, however, we report both, the most stable and the on-top binding energy, but we have limited the graphical depiction of binding sites in Fig. 6C to the most stable geometries only.

As we have observed for OH, the elevated outer Ru row is most reactive and binds CO stronger ($E_{CO,bridge} = -2.19$ eV, Fig. 6C(d), $E_{CO,top} = -2.12$ eV) than the lower laying inner Ru row ($E_{CO,bridge} = -1.85$ eV, Fig. 6C(f), $E_{CO,top}$ −1.67 eV). On $Ru_{central}$ we predict that CO binds to the top site with an intermediate binding energy of $E_{CO} = -1.95$ eV. Contrary to OH, the energy difference between CO adsorption on Ru_{center} and Ru_{inner} is only ca. 0.1 eV (0.28 eV for on-top adsorption only), and therefore much less pronounced. On the basis of these calculated adsorption energies, we can deduce that (i) the CO binding energy landscape across $RuPt_{ML\text{-}CE}$/Au(111) is relatively flat, (ii) CO binds preferentially to the Ru-Pt interface, and (iii) CO binding on the compressed $RuPt_{ML\text{-}CE}$/Au(111) cluster is unexpectedly stronger than on the equilibrated Pt(111) or Ru(111) reference surfaces. The former two results suggest that CO is relatively mobile on the surface and diffuses much more readily than OH in the radial direction to reach its preferred adsorption site at the Ru-Pt interface. The latter result confirms that geometry relaxation in high strain situations with weak ligand effects can become the dominant driver for changes in adsorption energy.

Table 1
Calculated CO and OH binding energies. Bolded values represent the most stable binding energies for Pt(111) and Ru(111). For $RuPt_{ML\text{-}CE}$/Au(111) the most stable sites on Pt and each Ru ring are given in bold face and correspond to the geometries shown in Fig. 6C.

Surface	Adsorption site	E_{CO} (eV)	E_{OH} (eV)
Pt(111)	top	−1.73	1.63
	bridge	−1.76	**0.63**
	fcc	**−1.78**	0.90
	hcp	−1.75	1.25
Ru(111)	top	**−1.74**	0.62
	bridge	−1.67	−0.04
	fcc	−1.50	**−0.10**
	hcp	−1.68	−0.05
$RuPt_{ML\text{-}CE}$/Au(111)	Pt_{top}	−2.02	0.38
	Pt_{bridge}	**−2.12**	**0.52**
	$Ru_{outer/top}$	−2.12	-
	$Ru_{outer/bridge}$	**−2.19**	**−0.83**
	$Ru_{inner/top}$	−1.67	-
	$Ru_{inner/bridge}$	**−1.85**	0.06
	Ru_{center}	**−1.95**	−0.56

4. Discussion

We used UPD and SLRR to synthesize a unique RuPt core-edge structure on Au(111), and confirmed its 2D geometry using STM. CV experiments demonstrate superior thermodynamic and kinetic CO oxidization behavior compared to the Ru_{ML}/Au(111) and Pt_{ML}/Au(111) catalysts (Fig. 4). The measured current density per atom is significantly higher than previously reported values [55]. This large activity increase is not easily explained, but insight into the atomic-scale relaxation and equilibrium structure in the context of the experimental observations and previous literature can elucidate some of the mechanistic details and provide a qualitative description of the dominant catalytic features of $RuPt_{ML\text{-}CE}$/Au(111).

For the mechanistic discussion we consider five key steps: (i) CO adsorption until saturation is reached; (ii) H_2O electro-oxidation and formation of adsorbed OH; (iii) displacement of CO with OH (does not contribute to CV signal); (iv) CO oxidation (contributes to CV signal); and (v) possible surface diffusion of CO and OH to active sites. Here, CO adsorption can be ruled out as differentiating step, because a CO saturated surface is the initial coverage in all cases. Certainly important, however, is the preference to displace CO versus CO oxidation as OH starts to form. Earlier work has shown that Ru(0001) has low activity for CO oxidation due to a strong Ru-OH interaction and non-reactive displacement of pre-adsorbed CO [60]. Hence, we may qualitatively conclude that on Ru the barrier for CO oxidation is larger than for H_2O oxidation and its CO oxidation activity measured in CV experiments

depends largely on the competitive adsorption between CO and OH. Pt(111) on the other hand, is easily saturated with CO and its activity is limited by H_2O oxidation and the availability of OH [54]. Finally, surface diffusion only plays a role where the catalyst has spatially distributed reactions sites, such as the RuPt core-edge nanoclusters.

We begin with a discussion of the competitive adsorption between CO and OH. For the sake of simplicity and ease of comparison with SNFTIRS data, we consider only on-top adsorption for CO and use the difference $\Delta E_{CO\text{-}OH} = E_{CO} - E_{OH}$ as indicator for preferential occupation of a site by CO or OH. A more negative value indicates a larger preference for CO adsorption. For Ru(111) we obtain $\Delta E_{CO\text{-}OH} = -1.64$ eV and for Pt(111) $\Delta E_{CO\text{-}OH} = -2.36$ eV. By comparison to the above mentioned experimental observations [54,60] we propose a rule of thumb stating that adsorption sites with $\Delta E_{CO\text{-}OH} < -2.3$ eV are preferentially occupied by CO and contribute to the measured CO oxidation current, whereas $\Delta E_{CO\text{-}OH} > -1.6$ eV indicates preferential coverage by OH and simple desorption of CO (no oxidation). For -2.3 eV $< \Delta E_{CO\text{-}OH} < -1.6$ eV we assume a mix of CO and OH coverage, as well as mixed CO desorption and oxidation.

The values of $\Delta E_{CO\text{-}OH}$ for $RuPt_{ML\text{-}CE}/Au(111)$ and the expected occupancy of each site are tabulated in Table 2. This qualitative and simplified analysis predicts that CO adsorbs preferentially on the Pt ring with a binding energy that is 0.29 eV stronger than on Pt(111). The Ru sites on elevated rings (Ru_{center}, Ru_{outer}) are covered by OH after CO displacement and also bind OH significantly more strongly than Ru(111). For the lower laying Ru sites (Ru_{inner}) $\Delta E_{CO\text{-}OH}$ is in between the limiting values established by Ru(111) and Pt(111) and we must assume mixed occupation with OH and CO. These sites also show generally weaker interactions with CO and OH compared to Ru(111), indicating a lower total coverage of these sites.

Our theoretical prediction of site occupation on $RuPt_{ML\text{-}CE}/Au(111)$ agrees well with the SNFTIRS data shown in Fig. 5. When no Pt sites are available, CO must adsorb on Ru sites, on which E_{CO} has an oscillating radial dependence. CO binds strongly to elevated rows, but weakly to low laying rows. This is reflected by the existence of multiple ν_{CO} peaks for $Ru_{ML}/Au(111)$ in our SNFTIRS data that correspond to strongly and weakly adsorbed CO molecules. If we also consider the preferential occupations predicted in Table 2, most CO is adsorbed on the weak binding Ru_{inner} sites where $E_{CO} = -1.67$ eV is weaker than on Ru(111), $E_{CO} = -1.74$. This is again consistent with the occurrence of the main ν_{CO} peak for $Ru_{ML}/Au(111)$ at higher wave numbers than on Ru(0001).

When Pt is present in the $RuPt_{ML\text{-}CE}/Au(111)$ system, CO preferentially adsorbs to the Pt belt, resulting in a single SNFTIRS peak that has a similar shape as in the case of $Pt_{ML}/Au(111)$. The observed shift of ν_{CO} from 2072 cm^{-1} on Pt(111) to 2047 cm^{-1} on $RuPt_{ML\text{-}CE}/Au(111)$ is consistent with the stronger calculated binding energy of CO on the Pt site of $RuPt_{ML\text{-}CE}/Au(111)$ compared to Pt(111). Overall, our theoretical and experimental data suggest that before the onset of CO oxidation the Pt sites of the $RuPt_{ML\text{-}CE}/Au(111)$ surface are saturated with CO. CO initially adsorbed on elevated Ru sites is displaced by OH and a smaller amount of CO can be found adjacent to OH species on Ru sites of lower laying Ru rings.

Table 2
Preferential coverage prediction based on $\Delta E_{CO\text{-}OH} = E_{CO} - E_{OH}$ comparison with Pt(111) and Ru(111). On top adsorption of CO is assumed unless otherwise noted.

Surface	Location	$\Delta E_{CO\text{-}OH} = E_{CO} - E_{OH}$ (eV)	Preferentially occupied by
Pt(111)	-	−2.36	CO
Ru(111)	-	−1.64	OH
$RuPt_{ML\text{-}CE}/Au(111)$	Pt	−2.40	CO
	Ru_{outer}	−1.29	OH
	Ru_{inner}	−1.73	OH/CO
		−1.91 (CO on bridge)	
	Ru_{center}	−1.39	OH

The CV behavior of CO oxidation on $RuPt_{ML\text{-}CE}/Au(111)$ in Fig. 4 can now be discussed in terms of the spatial site distribution and surface diffusion. As stated before, the near order of magnitude higher activity of $RuPt_{ML\text{-}CE}/Au(111)$ must be attributed to highly reactive sites at the Ru-Pt interface. At the beginning of the potential sweep the interface consists of CO on Pt sites in direct vicinity of OH species adsorbed on Ru and the reaction may proceed immediately. In contrast to $Pt_{ML}/Au(111)$, CO oxidation in this scenario is not limited by OH supply. The earlier reaction onset in the case of the wider Pt belt (Pt^{2+}) is likely related to weaker bound Pt-CO at the Ru-Pt interface. For a two (or more) Pt atom wide belt, Pt atoms at the interface have an average coordination number of 9 and are expected to be less reactive than Pt atoms directly at the edge, which have a coordination number of 7 [61]. This interpretation is consistent with the observation of the Pt oxidation/reduction cycle for $RuPt_{ML\text{-}CE}/Au(111)$ (Pt^{2+}), which indicates the preservation of Pt-like behavior.

Once the initial CO/OH at the interface is rapidly depleted, the oxidation reaction displays a current plateau in the CV graph, which is independent on the Pt belt width and indicates a transport limited process. Indeed, our DFT results indicate that there is a thermodynamic driving force for radial CO and OH diffusion from the core area towards the Ru-Pt interface, but the rippled cluster surface shown in Fig. 6B with strong and weak binding Ru rows slows the diffusion process. While CO has a small diffusion barrier, the diffusion barrier for OH was estimated to be at least 0.6 eV or higher. These largely immobile OH species on elevated Ru rows form concentric circles that trap CO in the Ru core area and cause the diffusion limited plateau region observed in the CV measurements.

As the potential reaches the potential of the main oxidation peak for $Ru_{ML}/Au(111)$ (ca. 290 mV) the Ru core region of $RuPt_{ML\text{-}CE}/Au(111)$ becomes active for CO oxidation, but with rather slow CO oxidation kinetics. Yet, the reaction onset in the Ru core region temporarily removes blocking OH species and allows mobile CO species to quickly migrate radially outwards to the strongly binding Ru-Pt interface. In the absence of transport limitations the CO oxidation reaction occurs rapidly at the Ru-Pt interface associated with a drastic increase in current density observed in the CV graph (Fig. 4). The described mechanism is consistent with all experimental observations and computational data. It is also a prototype example of a truly bi—functional mechanism in which Ru and Pt form an active interface and each component contributes an individual functionality.

5. Conclusions

Using a two-step process consisting of underpotential deposition techniques and surface limited red-ox replacement we have synthesized a novel 2D core-edge monolayer catalyst morphology. The core-edge nanoclusters are deposited on Au(111) and are composed of a Ru core surrounded by a Pt edge, $RuPt_{ML\text{-}CE}/Au(111)$. STM analysis confirms that the synthesized 2D core-edge nanoclusters are of monoatomic height and CV experiments confirm their superior CO electro-oxidation activity that exceeds the activity of $Ru_{ML}/Au(111)$ and $Pt_{ML}/Au(111)$ by nearly an order of magnitude. The unique catalytic activity of the $RuPt_{ML\text{-}CE}/Au(111)$ catalyst is explained in terms of its rich adsorption energy landscape, which is a direct result of the surface reconstruction of the Ru core to form concentric ripples. The ripple formation in this particular system is caused by a large epitaxial lattice mismatch, weak ligand effects, and strong finite size effects. The characteristics of the adsorption energy landscape of the rippled core-edge structure were determined by a combination of DFT calculations and SNFTIRS experiments and point towards thermodynamically favorable radial transport from the Ru core to the active Ru-Pt interface. In addition, the ripples lead to alternating strong and weak binding sites, which are likely populated with OH and an OH/CO adlayer, respectively. The diffusion of OH in the radial direction is slow, while CO is relatively mobile. Based on the experimental and computational data we propose

a mechanism in which immobile OH species prevent CO diffusion and cause a transport controlled current plateau in the CV graph at low potentials. At higher potentials the Ru core region becomes active for CO oxidation leading to temporary removal of OH. This allows rapid diffusion of CO in the Ru core region to the Ru-Pt interface, where it can rapidly react. The proposed mechanism is truly bi-functional with two spatially separated domains and a catalytically active interface site. We postulate that the investigated $RuPt_{ML\text{-}CE}$/Au(111) catalyst has (electrochemical) applications beyond CO oxidation, *e.g.* methanol oxidation, and that analogous core-edge structures with different metal components can be synthesized. Our synthesis technique for the preparation of this novel 2D morphology opens up a new and entirely unexplored design space for monolayer catalysts, specifically if a reaction can benefit from bi-functional catalytic behavior.

Acknowledgments

The experimental material is based upon work supported by the National Science Foundation under the contract CHE-0955922. LCG and HAD acknowledge financial support from the National Science Foundation and the U.S. Department of Energy under contract NSF/DOE CBET-1258688. Use of the computational resources at the Center for Nanoscale Materials was supported by the U.S. DOE, Office of Science, Office of Basic Energy Sciences, under contract no. DE-AC02-06CH11357. Additional computational resources were provided by the Center for Advanced Computing and Data Systems (CACDS) and the Research Computing Center (RCC) at the University of Houston.

Appendix A. Supplementary data

Supplementary data to this article can be found online at http://dx.doi.org/10.1016/j.susc.2015.03.021.

References

[1] J.L. Zhang, M.B. Vukmirovic, Y. Xu, M. Mavrikakis, R.R. Adžić, Angew. Chem. Int. Ed. 44 (2005) 2132.
[2] L.A. Kibler, A.M. El-Aziz, R. Hoyer, D.M. Kolb, Angew. Chem. Int. Ed. 44 (2005) 2080.
[3] J. Zhang, M.B. Vukmirovic, K. Sasaki, A.U. Nilekar, M. Mavrikakis, R.R. Adžić, J. Am. Chem. Soc. 127 (2005) 12480.
[4] J. Zhang, K. Sasaki, E. Sutter, R.R. Adžić, Science 315 (2007) 220 (80-.).
[5] A. Kowal, M. Li, M. Shao, K. Sasaki, M.B. Vukmirovic, J. Zhang, N.S. Marinkovic, P. Liu, A.I. Frenkel, R.R. Adžić, Nat. Mater. 8 (2009) 325.
[6] S.R. Brankovic, J.X. Wang, R.R. Adžić, Electrochem. Solid-State Lett. 4 (2001) A217.
[7] R. Adžić, J. Zhang, K. Sasaki, M. Vukmirovic, M. Shao, J. Wang, A. Nilekar, M. Mavrikakis, J. Valerio, F. Uribe, Top. Catal. 46 (2007) 249.
[8] K. Sasaki, J.X. Wang, H. Naohara, N. Marinkovic, K. More, H. Inada, R.R. Adžić, Electrochim. Acta 55 (2010) 2645.
[9] A. Nilekar, Y. Xu, J. Zhang, M. Vukmirovic, K. Sasaki, R. Adžić, M. Mavrikakis, Top. Catal. 46 (2007) 276.
[10] M.P. Hyman, J.W. Medlin, J. Phys. Chem. C 111 (2007) 17052.
[11] J.R. Kitchin, J.K. Nørskov, M.A. Barteau, J.G. Chen, Phys. Rev. Lett. 93 (2004) 4.
[12] J. Greeley, M. Mavrikakis, Nat. Mater. 3 (2004) 810.
[13] S. Alayoglu, A.U. Nilekar, M. Mavrikakis, B. Eichhorn, Nat. Mater. 7 (2008) 333.
[14] J. Knudsen, A.U. Nilekar, R.T. Vang, J. Schnadt, E.L. Kunkes, J.A. Dumesic, M. Mavrikakis, F. Besenbacher, J. Am. Chem. Soc. 129 (2007) 6485.
[15] M.P. Hyman, B.T. Loveless, J.W. Medlin, Surf. Sci. 601 (2007) 5382.
[16] N. Schumacher, K. Andersson, L.C. Grabow, M. Mavrikakis, J. Nerlov, I. Chorkendorff, Surf. Sci. 602 (2008) 702.
[17] P.A. Dowben, Surf. Sci. Rep. 40 (2000) 151.
[18] J. Greeley, J.K. Nørskov, M. Mavrikakis, Annu. Rev. Phys. Chem. 53 (2002) 319.
[19] M. Mavrikakis, B. Hammer, J.K. Nørskov, Phys. Rev. Lett. 81 (1998) 2819.
[20] A. Schlapka, M. Lischka, A. Gross, U. Käsberger, P. Jakob, Phys. Rev. Lett. 91 (2003) 016101.
[21] E. Kampshoff, E. Hahn, K. Kern, Phys. Rev. Lett. 73 (1994) 704.
[22] A. Ruban, B. Hammer, P. Stoltze, H.L. Skriver, J.K. Nørskov, J. Mol. Catal. A Chem. 115 (1997) 421.
[23] T. Bligaard, J.K. Nørskov, Electrochim. Acta 52 (2007) 5512.
[24] L. Grabow, Y. Xu, M. Mavrikakis, Phys. Chem. Chem. Phys. 8 (2006) 3369.
[25] J. Wintterlin, T. Zambelli, J. Trost, J. Greeley, M. Mavrikakis, Angew. Chem. Int. Ed. 42 (2003) 2850.
[26] S.R. Brankovic, J. McBreen, R.R. Adžić, J. Electroanal. Chem. 503 (2001) 99.
[27] S.-E. Bae, D. Gokcen, P. Liu, P. Mohammadi, S.R. Brankovic, Electrocatalysis 3 (2012) 203.
[28] A.A. Kolmakov, D.W. Goodman, Size Effects in Catalysis by Supported Metal Clusters, in: S.N. Khanna, A.W. Castleman (Eds.), Quantum Phenomena in Clusters and Nanostructures, Springer-Verlag GmbH & Co. KG, Berlin and Heidelberg 2003, p. 159.
[29] L. Li, A.H. Larsen, N.A. Romero, V.A. Morozov, C. Glinsvad, F. Abild-Pedersen, J. Greeley, K.W. Jacobsen, J.K. Nørskov, J. Phys. Chem. Lett. 4 (2013) 222.
[30] R. Kern, P. Müller, Surf. Sci. 392 (1997) 103.
[31] R. Loukrakpam, Q. Yuan, V. Petkov, L. Gan, S. Rudi, R. Yang, Y. Huang, S.R. Brankovic, P. Strasser, Phys. Chem. Chem. Phys. 16 (2014) 18866.
[32] D. Gokcen, Q. Yuan, S.R. Brankovic, J. Electrochem. Soc. 161 (2014) D3051.
[33] J. Greeley, M. Mavrikakis, Catal. Today 111 (2006) 52.
[34] S. Brankovic, J. Wang, R. Adžić, Surf. Sci. 474 (2001) L173.
[35] S.R. Brankovic, in: G. Kreysa, K. Ota, R.F. Savinell (Eds.), Encycl. Appl. Electrochem, Springer, New York 2014, p. 423.
[36] A.E. Ismail, G.S. Grest, M.J. Stevens, J. Chem. Phys. 125 (2006) 1.
[37] J. Hotlos, O.M. Magnussen, R.J. Behm, Surf. Sci. 335 (1995) 129.
[38] D. Gokcen, S.-E. Bae, S.R. Brankovic, J. Electrochem. Soc. 157 (2010) D582.
[39] A. Tripathi, The New Image Processing Algorithm for Qualitative and Quantitative STM Image Data Analysis, University of Houston, 2012.
[40] Q. Yuan, A. Tripathi, M. Slavkovic, S.R. Brankovic, Z. Phys. Chem. 226 (2012) 965.
[41] N. Otsu, IEEE Trans. Syst. Man Cybern. SMC-9 (1979) 62.
[42] N.S. Marinković, M. Hecht, J.S. Loring, W.R. Fawcett, Electrochim. Acta 41 (1996) 641.
[43] G. Kresse, J. Furthmüller, Phys. Rev. B Condens. Matter 54 (1996) 11169.
[44] G. Kresse, J. Furthmüller, Comput. Mater. Sci. 6 (1996) 15.
[45] P.E. Blöchl, Phys. Rev. B 50 (1994).
[46] G. Kresse, D. Joubert, Phys. Rev. B 59 (1999) 1758.
[47] B. Hammer, L.B. Hansen, J.K. Nørskov, Phys. Rev. B 59 (1999) 7413.
[48] M.J. Gillan, J. Phys. Condens. Matter 1 (1989) 689.
[49] S.R. Bahn, K.W. Jacobsen, Comput. Sci. Eng. 4 (2002) 56.
[50] B.D. Cullity, S.R. Stock, Elements of X-Ray Diffraction, 3rd edition Prentice Hall, Upper Saddle River, NJ, 2001.
[51] H.J. Monkhorst, J.D. Pack, Phys. Rev. B 13 (1976) 5188.
[52] L. Bengtsson, Phys. Rev. B 59 (1999) 12301.
[53] N. Ikemiya, T. Senna, M. Ito, Surf. Sci. 464 (2000).
[54] I. Villegas, M.J. Weaver, J. Chem. Phys. 101 (1994) 1648.
[55] P.N. Ross Jr., The Science of Electrocatalyis on Bimetallic Surfaces, in: J. Lipkowski, P.N. Ross (Eds.), Electrocatalysis, 1st ed.Wiley-VCH, New York 1998, p. 43.
[56] S.A. Wasileski, M.T.M. Koper, M.J. Weaver, J. Phys. Chem. B 105 (2001) 3518.
[57] P.J. Feibelman, B. Hammer, J.K. Nørskov, F. Wagner, M. Scheffler, R. Stumpf, R. Watwe, J. Dumesic, J. Phys. Chem. B 105 (2001) 4018.
[58] I. Grinberg, Y. Yourdshahyan, A.M. Rappe, J. Chem. Phys. 117 (2002) 2264.
[59] F. Abild-Pedersen, M.P. Andersson, Surf. Sci. 601 (2007) 1747.
[60] S.R. Brankovic, N.S. Marinkovic, J.X. Wang, R.R. Adžić, J. Electroanal. Chem. 532 (2002) 57.
[61] A.A. Peterson, L.C. Grabow, T.P. Brennan, B. Shong, C. Ooi, D.M. Wu, C.W. Li, A. Kushwaha, A.J. Medford, F. Mbuga, L. Li, J.K. Nørskov, Top. Catal. 55 (2012) 1276.